

Chapter 1

Theory of Passive Synthetic Aperture Imaging

Ling Wang, Can Evren Yarman and Birsen Yazıcı

Abstract We present a unified theory for passive synthetic aperture imaging based on inverse scattering, estimation-detection theory and microlocal analysis. Passive synthetic aperture imaging uses sources of opportunity for illumination and moving receivers to measure scattered field. We consider passive airborne receivers that fly along arbitrary, but known, flight trajectories and static or mobile sources of opportunity transmitting two types of waveforms: Single-frequency or ultra-narrowband Continuous-Wave (CW) waveforms and wideband pulsed waveforms. Our theory results in two new and novel synthetic aperture imaging modalities: *Doppler Synthetic Aperture Hitchhiker* (DSAH) that uses single-frequency or ultra-narrowband CW waveforms, and *Synthetic Aperture Hitchhiker* (SAH) that uses wideband pulsed waveforms. We use inverse scattering and estimation-detection theory to develop measurement models in the form of Fourier Integral Operators (FIOs) for DSAH and SAH. These models are based on windowed, scaled and translated correlations of the measurements from two different receiver locations. This processing removes the transmitter-related terms from the phase of the resulting FIOs that map the radiance of the scene to correlated measurements. We use microlocal analysis to develop approximate inversion formulas for these FIOs. The inversion formulas involve backprojection of the correlated measurements onto certain manifolds where the passive range and passive Doppler are constant for SAH and DSAH imaging, respectively. We present resolution analysis and numerical simulations to demonstrate our theoretical results. While we focus primarily on the passive synthetic aperture

Ling Wang

College of Electronic and Information Engineering, Nanjing University of Aeronautics and Astronautics, Nanjing, 210016, People's Republic of China e-mail: wanglrpi@gmail.com

Can Evren Yarman

WesternGeco-Schlumberger, Houston TX, 77042, USA e-mail: cyarman@slb.com

Birsen Yazıcı

Department of Electrical, Computer and System Engineering, Rensselaer Polytechnic Institute, Troy, NY 12180, USA e-mail: yazici@ecse.rpi.edu

radar, the theory we present is also applicable to other wave-based passive synthetic aperture imaging problems such as those in acoustics and geophysics.

1.1 Introduction

With the rapid growth of illumination sources of opportunity, such as broadcasting stations, mobile phone base stations, as well as relatively low cost and rapid deployment of receivers, there has been a growing interest in passive detection and imaging applications in recent years [1, 2, 5–7, 9–14, 17–20, 23, 27–29, 32, 36].

Most of the existing passive imaging methods are focused on the detection of scatterers with stationary receivers [2, 5–7, 9–14, 17–20, 27–29, 32, 36]. Recently, a number of methods for passive synthetic aperture were introduced [1, 23, 38, 39].

In this chapter, we presented a unified theory of passive synthetic aperture imaging based on inverse scattering theory, estimation-detection theory and microlocal analysis. Our theory facilitates resolution analysis and relates backprojection-based image reconstruction to statistical beamforming methods as well as to ambiguity theory [21, 22, 31, 34, 35, 37]. It is applicable to passive imaging with both cooperative and non-cooperative sources of illumination where the location of the sources and transmitted waveforms are unknown. The theory can be also viewed as a limiting case of the passive imaging and detection methods that we developed for sparsely distributed receivers [36]. It results in new and novel passive synthetic aperture imaging modalities [38, 39] with several advantages over the existing passive radar detection methods. (See [36, 38, 39] for a comparative review of related work.)

We consider multiple receivers moving along arbitrary, but known, trajectories over a non-flat topography and two types of illumination sources of opportunity: Single-frequency or ultra-narrowband Continuous-Wave (CW), and wideband pulsed waveforms of opportunity. Due to the high Doppler resolution nature of the single-frequency or ultra-narrowband CW waveforms, we refer to the modality that uses these waveforms as the *Doppler Synthetic Aperture Hitchhiker* (DSAH) [38]. Due to the high range resolution nature of the wideband pulsed waveforms, we refer to the modality that uses wideband pulsed waveforms as the *Range Synthetic Aperture Hitchhiker* or simply the *Synthetic Aperture Hitchhiker* (SAH) [39].

For each pair of receivers, we correlate the windowed signal obtained from one of the receivers with the *windowed, scaled and translated* version of the received signal from another receiver. We express the relationship between the scene radiance and the correlated measurements in the form of Fourier Integral Operators (FIOs). The correlation of received signals removes the transmitter related terms from the phase component of the resulting FIOs. As a result these FIOs can be inverted approximately by using microlocal techniques without the knowledge of the location of the transmitters. The DSAH measurement model does not rely on the start-stop approximation and is based on the fast-time Doppler, while the SAH measurement model relies on the start-stop approximation. In this context the SAH measurement

model can be derived from the DSAH measurement model by setting the fast-time Doppler variable to unity.

The high frequency analysis of the DSAH and SAH FIOs shows that the correlated measurements are the projections of the scene radiance onto the passive iso-Doppler and passive iso-range curves in DSAH and SAH imaging, respectively.

We use microlocal techniques to develop filtered-backprojection type approximate inversions of DSAH and SAH FIOs. The reconstructed images preserve the location and orientation of the visible edges of the scene radiance. Additionally, the reconstruction formulas can be implemented efficiently using the fast-backprojection algorithms [8]. Our unified approach to passive imaging readily facilitates resolution analysis that is consistent with the ambiguity theory [22, 31, 37].

While we focused primarily on passive synthetic aperture radar, the theory of DSAH and SAH imaging and the resulting methods and algorithms are also applicable to other wave-based passive imaging problems, such as those that arise in geophysics or acoustics.

The organization of the Chapter is as follows: In Section 1.2, we derive and analyze the leading order contributors of the measurement models for DSAH and SAH. In Section 1.3, we develop filtered-backprojection type image formation methods for DSAH and SAH, respectively. In Section 1.4, we analyze the resolution of DSAH and SAH imaging. In Section 1.5, we present numerical simulations to demonstrate the performance of the DSAH and SAH imaging methods. Finally, in Section 1.6 we conclude our discussion.

1.2 Measurement Model

We use the following notational conventions throughout the paper. The bold Roman, bold italic and Roman lower-case letters are used to denote variables in \mathbb{R}^3 , \mathbb{R}^2 and \mathbb{R} , respectively, i.e., $\mathbf{z} = (z, z) \in \mathbb{R}^3$, with $\mathbf{z} \in \mathbb{R}^2$ and $z \in \mathbb{R}$. The calligraphic letters (\mathcal{F} , \mathcal{H} etc.) are used to denote operators.

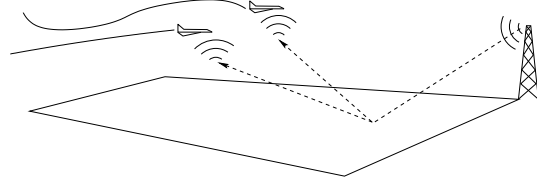
Given a pair of transmitter and receiver antennas located at \mathbf{T} and \mathbf{R} respectively, we model the received signal by [25]

$$\begin{aligned} f(t, \mathbf{R}, \mathbf{T}) \approx & \int \frac{e^{i\omega(t - (|\mathbf{R} - \mathbf{z}| + |\mathbf{z} - \mathbf{T}|)/c_0)}}{(4\pi)^2 |\mathbf{R} - \mathbf{z}| |\mathbf{z} - \mathbf{T}|} \omega^2 \hat{p}(\omega) \\ & \times J_{\text{tr}}(\omega, \widehat{\mathbf{z} - \mathbf{T}}, \mathbf{T}) J_{\text{rc}}(\omega, \widehat{\mathbf{z} - \mathbf{R}}, \mathbf{R}) V(\mathbf{z}) d\omega d\mathbf{z}, \end{aligned} \quad (1.1)$$

or in time-domain by

$$\begin{aligned} f(t, \mathbf{R}, \mathbf{T}) \approx & \int \frac{\ddot{p}(t - (|\mathbf{R} - \mathbf{z}| + |\mathbf{z} - \mathbf{T}|)/c_0)}{(4\pi)^2 |\mathbf{R} - \mathbf{z}| |\mathbf{z} - \mathbf{T}|} \\ & \times J_{\text{tr}}(\widehat{\mathbf{z} - \mathbf{T}}, \mathbf{T}) J_{\text{rc}}(\widehat{\mathbf{z} - \mathbf{R}}, \mathbf{R}) V(\mathbf{z}) d\mathbf{z}, \end{aligned} \quad (1.2)$$

Fig. 1.1 An illustration of the imaging geometry.



where t denotes time, c_0 denotes the speed of light in free space, $V(\mathbf{z})$ is the reflectivity function, \hat{p} denotes the Fourier transform the transmitted waveform, $p(t)$, J_{tr} and J_{rc} are the transmitter and receiver antenna beam pattern related terms, respectively.

We denote the earth's surface by $\mathbf{z} = (z, \psi(z)) \in \mathbb{R}^3$, where $z \in \mathbb{R}^2$ and $\psi : \mathbb{R}^2 \rightarrow \mathbb{R}$ is a known function for the ground topography. Furthermore, we assume that the scattering takes place in a thin region near the surface. Thus, the reflectivity function is in the form

$$V(\mathbf{z}) = \rho(z)\delta(z - \psi(z)). \quad (1.3)$$

Our passive imaging theory is applicable to both mobile and stationary sources of opportunity. However, for the rest of our discussion, we assume that there is a single, stationary transmitter of opportunity illuminating the scene. This allows us to simplify the analysis and distill the important aspects that can readily be generalized using the ideas similar to the ones presented in our work [39].

Let $\mathbf{T} \in \mathbb{R}^3$ denote the location of the transmitter of opportunity and let there be N airborne receivers, each traversing a smooth trajectory $\boldsymbol{\gamma}_i(t')$, $i = 1, \dots, N$ as shown in Figure 1.1. Then, we denote the received signal at the i th receiver starting at time $t' = s$ by

$$\begin{aligned} e_i(t+s) &= f(t+s, \boldsymbol{\gamma}_i(t+s), \mathbf{T}) \\ &= \int \frac{\ddot{p}(t+s - (|\boldsymbol{\gamma}_i(t+s) - \mathbf{z}| + |\mathbf{z} - \mathbf{T}|)/c_0)}{(4\pi)^2 |\boldsymbol{\gamma}_i(t+s) - \mathbf{z}| |\mathbf{z} - \mathbf{T}|} \\ &\quad \times J_{tr}(\widehat{\mathbf{z} - \mathbf{T}}, \mathbf{T}) J_{rc}(\widehat{\mathbf{z} - \boldsymbol{\gamma}_i(t+s)}, \boldsymbol{\gamma}_i(t+s)) \rho(\mathbf{z}) d\mathbf{z}. \end{aligned} \quad (1.4)$$

Note that the time variable t' represents the absolute time, while t represents the relative time within the time interval starting at $t' = s$.

For a finite and relatively short interval, we use the Taylor series expansion around $t = 0$,

$$\boldsymbol{\gamma}_i(t+s) = \boldsymbol{\gamma}_i(s) + \dot{\boldsymbol{\gamma}}_i(s)t + \dots \quad (1.5)$$

to approximate

$$|\boldsymbol{\gamma}_i(t+s) - \mathbf{z}| \approx |\boldsymbol{\gamma}_i(s) - \mathbf{z}| + \widehat{\boldsymbol{\gamma}_i(s) - \mathbf{z}} \cdot \dot{\boldsymbol{\gamma}}_i(s)t. \quad (1.6)$$

Substituting the approximation (1.6) into (1.4), we have

$$e_i(t+s) \approx \int \frac{\ddot{p}(\alpha_i(s, \mathbf{z})t+s - (|\boldsymbol{\gamma}_i(s) - \mathbf{z}| + |\mathbf{z} - \mathbf{T}|)/c_0)}{(4\pi)^2 |\boldsymbol{\gamma}_i(s) - \mathbf{z}| |\mathbf{z} - \mathbf{T}|} \times J_{\text{tr}}(\widehat{\mathbf{z} - \mathbf{T}}, \mathbf{T}) J_{\text{rc}}(\mathbf{z} - \widehat{\boldsymbol{\gamma}_i(t+s)}, \boldsymbol{\gamma}_i(t+s)) \rho(\mathbf{z}) d\mathbf{z}, \quad (1.7)$$

where the time dilation

$$\alpha_i(s, \mathbf{z}) = 1 - \frac{\widehat{\boldsymbol{\gamma}_i(s) - \mathbf{z}} \cdot \dot{\boldsymbol{\gamma}_i(s)}}{c_0} \quad (1.8)$$

is the Doppler-scale-factor induced by the movement of the i th receiver.

We define the *windowed, scaled-and-translated correlation* of the received signals e_i and e_j by

$$c_{ij}(s', s, \mu) = \int e_i(t+s') e_j^*(\mu t+s) \phi(t) dt, \quad (1.9)$$

for some $s, s' \in \mathbb{R}$ and $\mu \in \mathbb{R}^+$, $i, j = 1, \dots, N$, where $\phi(t)$ is a smooth compactly supported temporal windowing function centered at $t = 0$.

In the following subsections, we develop mappings that relate the expected value of the correlated measurements c_{ij} , denoted by $E[c_{ij}]$, to the scene to be imaged. We assume that the sources of opportunity are non-cooperative, where the location of the transmitter, \mathbf{T} , and transmitter antenna beam pattern related term J_{tr} are unknown.

We use a stochastic model for the transmitter antenna beam pattern related term, J_{tr} , and the scene reflectivity, ρ , and assume ρ and J_{tr} are statistically independent, to express $E[c_{ij}]$ as

$$E[c_{ij}](s', s, \mu) \approx \int \ddot{p}(\alpha_i(s, \mathbf{z})t+s' - (|\boldsymbol{\gamma}_i(s') - \mathbf{z}| + |\mathbf{z} - \mathbf{T}|)/c_0) \times \ddot{p}^*(\mu \alpha_j(s, \mathbf{z}')t+s - (|\boldsymbol{\gamma}_j(s) - \mathbf{z}'| + |\mathbf{z}' - \mathbf{T}|)/c_0) \times \frac{C_\rho(\mathbf{z}, \mathbf{z}') C_{J_{\text{tr}}}(\mathbf{z}, \mathbf{z}', \mathbf{T}) A_{R_{ij}}(\mathbf{z}, \mathbf{z}', t, s', s, \mu)}{(4\pi)^4 G_{ij}(\mathbf{z}, \mathbf{z}', s, s', \mu)} d\mathbf{z} d\mathbf{z}' \phi(t) dt. \quad (1.10)$$

C_ρ and $C_{J_{\text{tr}}}$ denote the correlation functions of ρ and J_{tr} , respectively, i.e.,

$$C_\rho(\mathbf{z}, \mathbf{z}') = E[\rho(\mathbf{z})\rho^*(\mathbf{z}')], \quad (1.11)$$

$$C_{J_{\text{tr}}}(\mathbf{z}, \mathbf{z}', \mathbf{T}) = E[J_{\text{tr}}(\widehat{\mathbf{z} - \mathbf{T}}, \mathbf{T}) J_{\text{tr}}^*(\widehat{\mathbf{z}' - \mathbf{T}}, \mathbf{T})]. \quad (1.12)$$

$A_{R_{ij}}$ denotes the product of the receiver antenna beam patterns,

$$A_{R_{ij}}(\mathbf{z}, \mathbf{z}', t, s', s, \mu) = J_{\text{rc}}(\mathbf{z} - \widehat{\boldsymbol{\gamma}_i(t+s')}, \boldsymbol{\gamma}_i(t+s')) \times J_{\text{rc}}^*(\mathbf{z}' - \widehat{\boldsymbol{\gamma}_j(\mu t+s)}, \boldsymbol{\gamma}_j(\mu t+s)), \quad (1.13)$$

and G_{ij} is the product of the geometric spreading factors,

$$G_{ij}(\mathbf{z}, \mathbf{z}', s', s) = |\mathbf{T} - \mathbf{z}| |\mathbf{T} - \mathbf{z}'| |\boldsymbol{\gamma}_i(s') - \mathbf{z}| |\boldsymbol{\gamma}_j(s) - \mathbf{z}'|. \quad (1.14)$$

Note that for non-cooperative sources of opportunity, \mathbf{T} , and thus $|\mathbf{T} - \mathbf{z}| |\mathbf{T} - \mathbf{z}'|$, are unknown. For the case of cooperative sources of opportunity where these quantities along with the transmitted antenna beam pattern are assumed to be known, (1.12) can be modified to include the known quantities.

Next, we make the incoherent-field approximation [3] by assuming that ρ and J_{tr} satisfy the following equalities:

$$C_\rho(\mathbf{z}, \mathbf{z}') = R_\rho(\mathbf{z}) \delta(\mathbf{z} - \mathbf{z}'), \quad (1.15)$$

$$C_{J_{tr}}(\mathbf{z}, \mathbf{z}', \mathbf{T}) = R_T(\mathbf{z}) \delta(\mathbf{z} - \mathbf{z}'). \quad (1.16)$$

R_ρ is the average power of the electromagnetic radiation emitted by the scene at location \mathbf{z} , and R_T is the average power of the electromagnetic radiation emitted by the transmitter at location \mathbf{T} that is incident on the target surface at \mathbf{z} . In this regard, R_ρ is referred to as the *scene radiance* and R_T is referred to as the transmitter irradiance [3].

Substituting (1.15) and (1.16) into (1.10), we obtain

$$\begin{aligned} E[c_{ij}](s', s, \mu) &= \int \ddot{p}(\alpha_i(s', \mathbf{z})t + s' - (|\boldsymbol{\gamma}_i(s') - \mathbf{z}| + |\mathbf{z} - \mathbf{T}|)/c_0) \\ &\quad \times \ddot{p}^*(\mu\alpha_j(s, \mathbf{z})t + s - (|\boldsymbol{\gamma}_j(s) - \mathbf{z}| + |\mathbf{z} - \mathbf{T}|)/c_0) \\ &\quad \times \frac{R_\rho(\mathbf{z})R_T(\mathbf{z})A_{R_{ij}}(\mathbf{z}, \mathbf{z}, t, s', s, \mu)}{(4\pi)^4 G_{ij}(\mathbf{z}, \mathbf{z}, s, s', \mu)} d\mathbf{z} \phi(t) dt \end{aligned} \quad (1.17)$$

for some $s, s' \in \mathbb{R}$, $\mu \in \mathbb{R}^+$ and $i, j = 1, \dots, N$. We refer to (1.17) as the correlated measurements.

Our objective is to determine the scene radiance R_ρ given $E[c_{ij}](s', s, \mu)$ for a range of s', s and μ . In the following two subsections, we study two special cases of the measurement model to derive the measurement models for the DSAH and SAH.

1.2.1 Model for Doppler Synthetic Aperture Hitchhiker Imaging

In DSAH, narrowband or ultra-narrowband CW waveforms of opportunity are used for imaging. Thus,

$$p(t) = e^{i\omega_0 t} \tilde{p}(t), \quad (1.18)$$

where ω_0 denotes the carrier frequency and $\tilde{p}(t)$ is the complex envelope of p , which is a slow varying function of t as compared to $e^{i\omega_0 t}$.

Substituting (1.18) into (1.17), we express $E[c_{ij}]$ as

$$\begin{aligned}
E[c_{ij}(s', s, \mu)] &= \frac{\omega_0^4}{(4\pi)^4} \int e^{i\omega_0(\alpha_i(s', \mathbf{z})t + s' - (|\boldsymbol{\gamma}_i(s') - \mathbf{z}| + |\mathbf{T} - \mathbf{z}|)/c_0)} \\
&\quad \times e^{-i\omega_0(\mu\alpha_j(s, \mathbf{z})t + s - (|\boldsymbol{\gamma}_j(s) - \mathbf{z}| + |\mathbf{T} - \mathbf{z}|)/c_0)} \\
&\quad \times \frac{R_T(\mathbf{z})A_{\bar{p}}(\mathbf{z}, \mathbf{z}, t, s', s, \mu)A_{R_{ij}}(\mathbf{z}, \mathbf{z}, t, s', s, \mu)}{G_{ij}(\mathbf{z}, \mathbf{z}, s', s, \mu)} \\
&\quad \times R_\rho(\mathbf{z})d\mathbf{z}\phi(t)dt, \tag{1.19}
\end{aligned}$$

where $A_{\bar{p}}$ is the product of the complex envelope of the transmitted waveform,

$$\begin{aligned}
A_{\bar{p}} &= \bar{p}(\alpha_i(s', \mathbf{z})t + s' - (|\boldsymbol{\gamma}_i(s') - \mathbf{z}| + |\mathbf{T} - \mathbf{z}|)/c_0) \\
&\quad \times \bar{p}^*(\mu\alpha_j(s, \mathbf{z})t + s - (|\boldsymbol{\gamma}_j(s) - \mathbf{z}| + |\mathbf{T} - \mathbf{z}'|)/c_0). \tag{1.20}
\end{aligned}$$

After rearranging the terms in (1.19), we have

$$\begin{aligned}
E[c_{ij}(s', s, \mu)] &\approx \mathcal{F}_{ij}^{\text{DSAHA}}[R_\rho](s', s, \mu) \\
&= \int e^{-i\phi_{ij}^{\text{DSAHA}}(t, \mathbf{z}, s', s, \mu)} A_{ij}^{\text{DSAHA}}(\mathbf{z}, t, s', s, \mu) R_\rho(\mathbf{z})d\mathbf{z}dt, \tag{1.21}
\end{aligned}$$

where

$$\phi_{ij}^{\text{DSAHA}}(t, \mathbf{z}, s', s, \mu) = \omega_0\alpha_j(s, \mathbf{z})t [\mu - S_{ij}(s', s, \mathbf{z})], \tag{1.22}$$

with

$$S_{ij}(s', s, \mathbf{z}) = \frac{\alpha_i(s', \mathbf{z})}{\alpha_j(s, \mathbf{z})} = \frac{1 - (\widehat{\boldsymbol{\gamma}_i(s') - \mathbf{z}}) \cdot \widehat{\boldsymbol{\gamma}_i(s')}/c_0}{1 - (\widehat{\boldsymbol{\gamma}_j(s) - \mathbf{z}}) \cdot \widehat{\boldsymbol{\gamma}_j(s)}/c_0}, \tag{1.23}$$

and

$$\begin{aligned}
A_{ij}^{\text{DSAHA}}(\mathbf{z}, t, s', s, \mu) &= \frac{\omega_0^4 R_T(\mathbf{z})A_{\bar{p}}(\mathbf{z}, \mathbf{z}, t, s', s, \mu)A_{R_{ij}}(\mathbf{z}, \mathbf{z}, t, s', s, \mu)\phi(t)}{(4\pi)^4 G_{ij}(\mathbf{z}, \mathbf{z}, t, s', s, \mu)} \\
&\quad \times e^{i\omega_0(s' - s - (|\boldsymbol{\gamma}_i(s') - \mathbf{z}| - |\boldsymbol{\gamma}_j(s) - \mathbf{z}|)/c_0)}. \tag{1.24}
\end{aligned}$$

We refer to $S_{ij}(s', s, \mathbf{z})$ as the *Doppler-hitchhiker-scale-factor*.

For cooperative sources of opportunity, where the transmitter locations and antenna beam patterns are assumed to be known, we treat J_{tr} deterministically and replace $R_T(\mathbf{z})$ with $J_{\text{tr}}(\widehat{\mathbf{z} - \mathbf{T}}, \mathbf{T})J_{\text{tr}}^*(\widehat{\mathbf{z} - \mathbf{T}}, \mathbf{T})$.

We refer to $\mathcal{F}_{ij}^{\text{DSAHA}}$ defined in (1.21) as the DSAH or *Doppler-hitchhiker FIO*; and ϕ_{ij}^{DSAHA} , A_{ij}^{DSAHA} as the phase and amplitude terms of the operator $\mathcal{F}_{ij}^{\text{DSAHA}}$.

Note that the scaled-and-translated correlation of the received signal removes all transmitter related terms from the phase of the operator $\mathcal{F}_{ij}^{\text{DSAHA}}$.

High Frequency Analysis of the DSAH FIO and Passive iso-Doppler Contours

We assume that for some m_A^{DSAH} , A_{ij}^{DSAH} satisfy the inequality

$$\sup_{(t,\mu,s',s,\mathbf{z}) \in U_{DSAH}} \left| \partial_t^{\alpha_t} \partial_\mu^{\alpha_\mu} \partial_{s'}^{\beta_1} \partial_s^{\beta_2} \partial_{z_1}^{\varepsilon_1} \partial_{z_2}^{\varepsilon_2} A_{ij}^{DSAH}(\mathbf{z}, t, s', s, \mu) \right| \leq C_A^{DSAH} (1+t^2)^{(m_A^{DSAH}-|\alpha_t|)/2}, \quad (1.25)$$

where U_{DSAH} is any compact subset of $\mathbb{R} \times \mathbb{R}^+ \times \mathbb{R} \times \mathbb{R} \times \mathbb{R}^2$ and the constant C_A^{DSAH} depends on U_{DSAH} , $\alpha_t, \mu, \beta_{1,2}$ and $\varepsilon_{1,2}$. In practice, (1.25) is satisfied for transmitters and receivers are sufficiently far away from the illuminated region.

Under the assumption (1.25), (1.21) defines \mathcal{F}_{ij}^{DSAH} as an FIO whose leading-order contributions come from those points lying in the intersection of the illuminated surface $(\mathbf{z}, \psi(\mathbf{z}))$ and points that have the same Doppler-hitchhiker-scale-factor, i.e., $\{\mathbf{z} \in \mathbb{R}^3 : S_{ij}(\tau', \tau, \mathbf{z}) = \mu\}$. We denote the curves formed by this intersection by

$$F_{ij}^{DSAH}(s', s, \mu) = \{\mathbf{z} : S_{ij}(s', s, \mathbf{z} = (\mathbf{z}, \psi(\mathbf{z}))) = \mu\}. \quad (1.26)$$

When the speed of the receivers is much slower than the speed of light c_0 , S_{ij} can be approximated as follows:

$$\begin{aligned} S_{ij}(s', s, \mathbf{z}) &= 1 + \frac{(\widehat{\boldsymbol{\gamma}_j(s)} - \mathbf{z}) \cdot \dot{\boldsymbol{\gamma}}_j(s)/c_0 - (\widehat{\boldsymbol{\gamma}_i(s')} - \mathbf{z}) \cdot \dot{\boldsymbol{\gamma}}_i(s')/c_0}{1 - (\widehat{\boldsymbol{\gamma}_j(s)} - \mathbf{z}) \cdot \dot{\boldsymbol{\gamma}}_j(s)/c_0} \\ &\approx 1 + [(\widehat{\boldsymbol{\gamma}_j(s)} - \mathbf{z}) \cdot \dot{\boldsymbol{\gamma}}_j(s) - (\widehat{\boldsymbol{\gamma}_i(s')} - \mathbf{z}) \cdot \dot{\boldsymbol{\gamma}}_i(s')]/c_0. \end{aligned} \quad (1.27)$$

Substituting (1.27) into

$$S_{ij}(s', s, \mathbf{z}) = \mu, \quad (1.28)$$

multiplying both sides of (1.28) by ω_0 , and rearranging the terms, we have

$$\frac{\omega_0}{c_0} \left[(\widehat{\boldsymbol{\gamma}_i(s')} - \mathbf{z}) \cdot \dot{\boldsymbol{\gamma}}_i(s') - (\widehat{\boldsymbol{\gamma}_j(s)} - \mathbf{z}) \cdot \dot{\boldsymbol{\gamma}}_j(s) \right] = (1 - \mu)\omega_0, \quad (1.29)$$

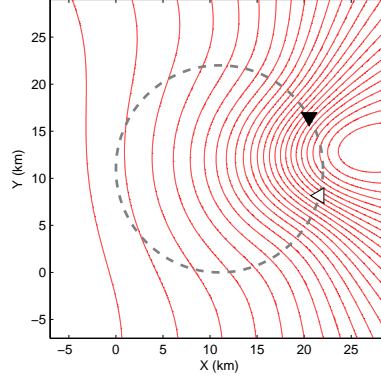
where the left hand side of (1.29) is the hitchhiker Doppler defined in [39] for a fixed frequency. In this regard, we refer to $F_{ij}^{DSAH}(s', s, \mu)$ as the passive iso-Doppler or *DSAH iso-Doppler* contour. Figure 1.2 shows the DSAH iso-Doppler contours for two receivers traversing a circular trajectory over a flat topography.

1.2.2 Model for Synthetic Aperture Hitchhiker Imaging

In SAH, wideband pulsed waveforms of opportunity are used for imaging.

Assuming that the velocity, $\dot{\boldsymbol{\gamma}}_j$ s, of the receivers are much less than the speed of light, we use the “start-stop” approximation, where the receiver is assumed to be stationary within a certain window of time, and approximate the Doppler-scale

Fig. 1.2 DSAH Iso-Doppler contours $F_{12}(s', s, \mu)$ for the Doppler-hitchhiker-scale-factor $S_{12}(22.0674s, -11.0337s, \mathbf{z})$. Two receivers are traversing a circular flight trajectory (dashed line) at the speed of 261 m/s over a flat topography. $\boldsymbol{\gamma}_1(\bar{s}) = \boldsymbol{\gamma}_C(\bar{s})$ and $\boldsymbol{\gamma}_2(\bar{s}) = \boldsymbol{\gamma}_C(\bar{s} - \pi/4)$, respectively, where white and black triangles denote the positions of the two receivers at $\bar{s} = \pi/6$, respectively. (See (1.23) and (1.70) for explicit formulae of $S_{12}(22.0674s, -11.0337s, \mathbf{z})$ and $\boldsymbol{\gamma}_C(\bar{s})$, respectively.)



factor

$$\alpha_i(s, \mathbf{z}) \approx 1. \quad (1.30)$$

Then the received signal at the i th receiver starting at time $t' = s'$ is approximated by

$$e_i(t + s') \approx \int \frac{\ddot{p}(t + s' - (|\boldsymbol{\gamma}_i(s') - \mathbf{z}| + |\mathbf{z} - \mathbf{T}|)/c_0)}{(4\pi)^2 |\boldsymbol{\gamma}_i(s') - \mathbf{z}| |\mathbf{z} - \mathbf{T}|} \times J_{\text{tr}}(\widehat{\mathbf{z} - \mathbf{T}}, \mathbf{T}) J_{\text{rc}}(\widehat{\mathbf{z} - \boldsymbol{\gamma}_i(s')}, \boldsymbol{\gamma}_i(s')) \rho(\mathbf{z}) d\mathbf{z}. \quad (1.31)$$

Similarly, under the start-stop approximation, the Doppler-hitchhiker-scale-factor becomes

$$S_{ij}(s', s, \mathbf{z}) \approx (1 - \alpha_i(s', \mathbf{z})) (1 + \alpha_j(s, \mathbf{z})) \approx 1. \quad (1.32)$$

Consequently, by (1.28), it is sufficient to consider $E[c_{ij}]$ for $\mu = 1$.

In this regard, taking into account the high range resolution of the wideband waveforms, we incorporate the fast-time delay in the forward model of SAH and define

$$d_{ij}(s', s, \tau) = c_{ij}(s', s - \tau, 1) = \int e_i(t + s') e_j^*(t + s - \tau) \phi(t) dt. \quad (1.33)$$

We refer to (1.33) as the *spatio-temporal correlation* of e_i and e_j .

Using (1.31), we approximate the expectation of $d_{ij}(s', s, \tau)$ as

$$E[d_{ij}(s', s, \tau)] = \int \ddot{p}(t + s' - (|\boldsymbol{\gamma}_i(s') - \mathbf{z}| + |\mathbf{z} - \mathbf{T}|)/c_0)$$

$$\begin{aligned}
& \times \ddot{p}^*(t+s-\tau - (|\boldsymbol{\gamma}_j(s) - \mathbf{z}| + |\mathbf{z} - \mathbf{T}|)/c_0) \\
& \times \frac{R_\rho(\mathbf{z})R_T(\mathbf{z})\tilde{A}_{R_{ij}}(\mathbf{z}, \mathbf{z}, s', s)}{(4\pi)^4 G_{ij}(\mathbf{z}, \mathbf{z}, s', s)} d\mathbf{z} \phi(t) dt \\
& = \int e^{i\omega(t+s' - (|\boldsymbol{\gamma}_i(s') - \mathbf{z}| + |\mathbf{z} - \mathbf{T}|)/c_0)} \\
& \times e^{-i\omega(t+s-\tau - (|\boldsymbol{\gamma}_j(s) - \mathbf{z}| + |\mathbf{z} - \mathbf{T}|)/c_0)} \\
& \times \frac{\omega^2 |\hat{p}(\omega)|^2 R_\rho(\mathbf{z})R_T(\mathbf{z})\tilde{A}_{R_{ij}}(\mathbf{z}, \mathbf{z}, s', s)}{(4\pi)^4 G_{ij}(\mathbf{z}, \mathbf{z}, s, s')} d\mathbf{z} d\omega \phi(t) dt \quad (1.34)
\end{aligned}$$

where

$$\tilde{A}_{R_{ij}}(\mathbf{z}, \mathbf{z}', s', s) = A_{R_{ij}}(\mathbf{z}, \mathbf{z}', 0, s', s, 1) \quad (1.35)$$

and $A_{R_{ij}}$ and G_{ij} are as in (1.13) and (1.14). We write

$$\begin{aligned}
E[d_{ij}(s', s, \tau)] & \approx \mathcal{F}_{ij}^{\text{SAH}}[R_\rho](s, s', \tau) \\
& = \int e^{-i\varphi_{ij}^{\text{SAH}}(\omega, \mathbf{z}, s, s', \tau)} A_{ij}^{\text{SAH}}(\mathbf{z}, \omega, s, s') R_\rho(\mathbf{z}) d\mathbf{z} dt, \quad (1.36)
\end{aligned}$$

where

$$\varphi_{ij}^{\text{SAH}}(\omega, \mathbf{z}, s', s, \tau) = \omega[r_{ij}(s', s, \mathbf{z})/c_0 + s - s' - \tau], \quad (1.37)$$

with

$$r_{ij}(s', s, \mathbf{z}) = |\boldsymbol{\gamma}_i(s') - \mathbf{z}| - |\boldsymbol{\gamma}_j(s) - \mathbf{z}| \quad (1.38)$$

and

$$A_{ij}^{\text{SAH}}(\mathbf{z}, \omega, s', s) = \frac{\omega^4 |\hat{p}(\omega)|^2 R_T(\mathbf{z})\tilde{A}_{R_{ij}}(\mathbf{z}, \mathbf{z}, s', s) \phi(t)}{(4\pi)^4 G_{ij}(\mathbf{z}, \mathbf{z}, s', s)}. \quad (1.39)$$

We refer to $r_{ij}(s', s, \mathbf{z})$ as the *hitchhiker or passive range*.

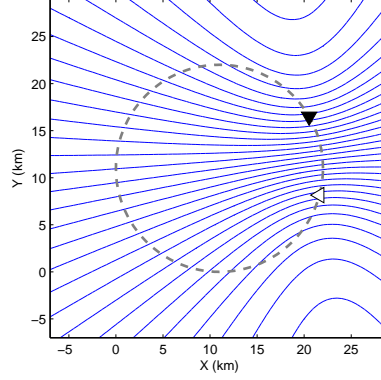
We remark that under the start-stop approximation $\varphi_{ij}^{\text{DSA}} \approx 1$ and $\varphi_{ij}^{\text{SAH}}$ is given by the exponential term in A_{ij}^{DSA} (see (1.24)), where s is replaced with $s - \tau$ in SAH to incorporate the fast-time delay information.

Similar to DSAH, for cooperative sources of opportunity, we treat J_{tr} deterministically and replace $\tilde{R}_T(\mathbf{z})$ with $J_{\text{tr}}(\widehat{\mathbf{z} - \mathbf{T}}, \mathbf{T})J_{\text{tr}}^*(\widehat{\mathbf{z} - \mathbf{T}}, \mathbf{T})$.

We refer to $\mathcal{F}_{ij}^{\text{SAH}}$ defined in (1.36) as the SAH or *range hitchhiker* or simply hitchhiker FIO; and $\varphi_{ij}^{\text{SAH}}$, A_{ij}^{SAH} as the phase and amplitude terms of the operator $\mathcal{F}_{ij}^{\text{SAH}}$.

Note that the spatio-temporal correlation of the received signal removes all transmitter related terms from the phase of the operator $\mathcal{F}_{ij}^{\text{SAH}}$.

Fig. 1.3 SAH Iso-range contours $H_{12}(s', s, C)$ for the hitchhiker range $r_{12}(22.0674s, -11.0337s, \mathbf{z})$. Two receivers are traversing a circular flight trajectory (dashed line) at the speed of 261 m/s over a flat topography. $\gamma_1(\bar{s}) = \gamma_C(\bar{s})$ and $\gamma_2(\bar{s}) = \gamma_C(\bar{s} - \pi/4)$, respectively, where white and black triangles denote the positions of the two receivers at $\bar{s} = \pi/6$, respectively. (See (1.38) and (1.70) for explicit formulae of $r_{12}(22.0674s, -11.0337s, \mathbf{z})$ and $\gamma_C(\bar{s})$, respectively.)



High Frequency Analysis of the SAH FIO and Passive iso-Range Contours

We assume that for some m_A^{SAH} , A_{ij}^{SAH} satisfy the inequalities

$$\sup_{(\omega, s', s, \mathbf{z}) \in U_{SAH}} \left| \partial_{\omega}^{\alpha_{\omega}} \partial_{s'}^{\beta_1} \partial_s^{\beta_2} \partial_{z_1}^{\varepsilon_1} \partial_{z_2}^{\varepsilon_2} A_{ij}^{SAH}(\mathbf{z}, \omega, s', s) \right| \leq C_A^{SAH} (1 + \omega^2)^{(m_A^{SAH} - |\alpha_{\omega}|)/2}, \quad (1.40)$$

where U_{SAH} is any compact subset of $\mathbb{R} \times \mathbb{R} \times \mathbb{R} \times \mathbb{R}^2$; the constant C_A^{SAH} depends on U_{SAH} , α_{ω} , $\beta_{1,2}$, $\varepsilon_{1,2}$. These assumptions are needed to make various stationary phase calculations hold. In practice, (1.40) is satisfied for transmitters and receivers sufficiently far away from the illuminated region.

Under the assumption (1.40), (1.36) defines \mathcal{F}_{ij}^{SAH} as an FIO whose leading-order contribution comes from those points lying at the intersection of the illuminated surface and the hyperboloid $\{\mathbf{x} \in \mathbb{R}^3 : r_{ij}(s', s, \mathbf{z}) = c_0(\tau + s' - s)\}$. We denote the curves formed by this intersection by

$$H_{ij}(s', s, \tau) = \{\mathbf{z} : r_{ij}(s', s, \mathbf{z}) = c_0(\tau + s' - s)\} \quad (1.41)$$

and refer to $H_{ij}(s', s, \tau)$ as the passive iso-range or *SAH iso-range* contour. For flat topography, $\psi(\mathbf{z}) = 0$, the SAH iso-range contours are given by hyperbolas on the plane $z_3 = 0$. We present the iso-range contours for circular receiver flight trajectories over a flat topography in Figure 1.3.

Comparing the DSAH and SAH presented in subsection 1.2.1 and subsection 1.2.2, we see that the DSAH imaging does not rely on the start-stop approximation and is based on the fast-time Doppler. In other words, the DSAH imaging method takes into account range variations or Doppler induced due to the movement of the

receivers during the reception of a CW waveform. SAH imaging, on the other hand, relies on the start-stop approximation and ignores the range variation due to the movement of the receivers, hence the fast-time Doppler, during the reception of a wideband pulse. Thus, the SAH measurement model can be derived from the DSAH measurement model by setting the Doppler-scale-factor to unity and decoupling the time into fast- and slow-time variables.

1.3 Image Formation

Our objective is to form an image of the scene radiance $R_\rho(\mathbf{z})$ using $E[c_{ij}(s', s, \mu)]$ or $E[d_{ij}(s', s, \tau)]$, $i, j = 1, \dots, N$ based on the correlated measurement models (1.21) for DSAH or (1.36) for SAH, respectively.

Since both \mathcal{F}_{ij}^{DSAH} and \mathcal{F}_{ij}^{SAH} are FIOs, we form an image of the scene radiance by other suitably designed Fourier integral operators FIOs, which we refer to as the *filtered-backprojection* operators. For DSAH, we backproject $E[c_{ij}(s', s, \mu)]$ onto passive iso-Doppler contours defined by $F_{ij}(s', s, \mu)$. For SAH, we backproject $E[d_{ij}(s', s, \tau)]$ onto passive iso-range contours defined by $H_{ij}(s', s, \tau)$ for $i, j = 1, \dots, N$. We form an image of the scene radiance by the superposition of the filtered and backprojected data.

1.3.1 DSAH Filtered-Backprojection Operator

For DSAH image formation, we invert $E[c_{ij}(s', s, \mu)]$ as follows:

$$\tilde{R}_\rho^{DSAH}(\mathbf{z}) = \sum_{ij} \int \mathcal{K}_{ij}^{DSAH}[E[c_{ij}]](\mathbf{z}, s') ds', \quad (1.42)$$

where we define

$$\mathcal{K}_{ij}^{DSAH}[E[c_{ij}]](\mathbf{z}, s') = \int e^{i\phi_{ij}^{DSAH}(t, \mathbf{z}, s', s, \mu)} Q_{ij}^{DSAH}(\mathbf{z}, t, s', s) E[c_{ij}(s', s, \mu)] dt ds d\mu. \quad (1.43)$$

We refer to \mathcal{K}_{ij}^{DSAH} as the DSAH filtered-backprojection operator with respect to the i th and j th receivers with filter Q_{ij}^{DSAH} to be determined below.

We assume that for some m_Q^{DSAH} , Q_{ij}^{DSAH} satisfies the inequality

$$\sup_{(t, s', s, \mathbf{z}) \in K_{DSAH}} \left| \partial_t^{\alpha_t} \partial_{s'}^{\beta_1} \partial_s^{\beta_2} \partial_{z_1}^{\varepsilon_1} \partial_{z_2}^{\varepsilon_2} Q_{ij}^{DSAH}(\mathbf{z}, t, s', s) \right| \leq C_Q^{DSAH} (1+t^2)^{(m_Q^{DSAH} - |\alpha_t|)/2}, \quad (1.44)$$

where $K_{DSA H}$ is any compact subsets of $\mathbb{R} \times \mathbb{R} \times \mathbb{R} \times \mathbb{R}^2$, and the constant $C_Q^{DSA H}$ depends on $K_{DSA H}, \alpha_t, \beta_{1,2}, \epsilon_{1,2}$. The assumption in (1.44) makes $\mathcal{K}_{ij}^{DSA H}$ an FIO.

Substituting (1.21) into (1.43) and the result back into (1.42), we obtain

$$\begin{aligned} \tilde{R}_\rho^{DSA H}(\mathbf{z}) &= \sum_{ij} \mathcal{K}_{ij}^{DSA H} \mathcal{F}_{ij}^{DSA H}[R_\rho](\mathbf{z}) \\ &= \int e^{i[\varphi_{ij}^{DSA H}(t, \mathbf{z}, s', s, \mu) - \varphi_{ij}^{DSA H}(t', \mathbf{z}', s', s, \mu)]} Q_{ij}^{DSA H}(\mathbf{z}, t, s', s) \\ &\quad \times A_{ij}^{DSA H}(\mathbf{z}', t, s', s, \mu) R_\rho(\mathbf{z}') dt' dt ds ds' d\mu dz'. \end{aligned} \quad (1.45)$$

We use the stationary phase theorem to approximate the t' and μ integrations [4, 15, 16, 24] and obtain

$$\begin{aligned} \tilde{R}_\rho^{DSA H}(\mathbf{z}) &\approx \sum_{ij} \int e^{i\omega_0 t [1 - (\widehat{\boldsymbol{\gamma}_j(s) - \mathbf{z}}) \cdot \dot{\boldsymbol{\gamma}}_j(s) / c_0] [S_{ij}(s', s, \mathbf{z}') - S_{ij}(s', s, \mathbf{z})]} \\ &\quad \times Q_{ij}^{DSA H}(\mathbf{z}, t, s', s) A_{ij}^{DSA H}(\mathbf{z}', t, s', s, S_{ij}(s', s, \mathbf{z}')) R_\rho(\mathbf{z}') dt ds ds' dz'. \end{aligned} \quad (1.46)$$

We linearize $S_{ij}(s', s, \mathbf{z}')$ around $\mathbf{z}' = \mathbf{z}$ and approximate

$$S_{ij}(\boldsymbol{\tau}', \boldsymbol{\tau}, \mathbf{z}') - S_{ij}(\boldsymbol{\tau}', \boldsymbol{\tau}, \mathbf{z}) \approx (\mathbf{z}' - \mathbf{z}) \cdot \nabla_{\mathbf{z}} S_{ij}(\boldsymbol{\tau}', \boldsymbol{\tau}, \mathbf{z}). \quad (1.47)$$

Let

$$\begin{aligned} \Xi_{ij}^{DSA H}(s', s, \mathbf{z}) &= \omega_0 [1 - (\widehat{\boldsymbol{\gamma}_j(s) - \mathbf{z}}) \cdot \dot{\boldsymbol{\gamma}}_j(s) / c_0] \nabla_{\mathbf{z}} S_{ij}(s', s, \mathbf{z}) \\ &= \frac{\omega_0}{c_0} D\psi(\mathbf{z}) \cdot \left[\frac{1}{|\boldsymbol{\gamma}_i(s') - \mathbf{z}|} \dot{\boldsymbol{\gamma}}_{i,\perp}(s') - \frac{S_{ij}(s', s, \mathbf{z})}{|\boldsymbol{\gamma}_j(s) - \mathbf{z}|} \dot{\boldsymbol{\gamma}}_{j,\perp}(s) \right], \end{aligned} \quad (1.48)$$

where

$$D\psi(\mathbf{z}) = \begin{bmatrix} 1 & 0 & \partial\psi(\mathbf{z})/\partial z_1 \\ 0 & 1 & \partial\psi(\mathbf{z})/\partial z_2 \end{bmatrix} \quad (1.49)$$

and $\dot{\boldsymbol{\gamma}}_{i,\perp}(s')$, $\dot{\boldsymbol{\gamma}}_{j,\perp}(s)$ are the projections of $\dot{\boldsymbol{\gamma}}_i(s')$ and $\dot{\boldsymbol{\gamma}}_j(s)$ onto the planes whose normal vectors are $(\widehat{\boldsymbol{\gamma}_i(s') - \mathbf{z}})$ and $(\widehat{\boldsymbol{\gamma}_j(s) - \mathbf{z}})$, respectively.

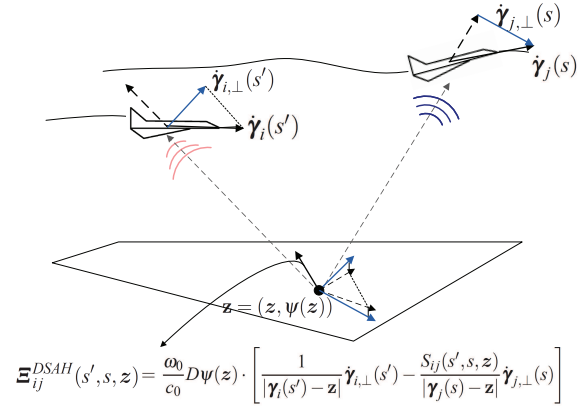
We show an illustration of the vector $\Xi_{ij}^{DSA H}(s', s, \mathbf{z})$ in Figure (1.4) for two receivers flying over a flat topography.

Substituting (1.47) and (1.48) into (1.46), we obtain

$$\begin{aligned} \tilde{R}_\rho^{DSA H}(\mathbf{z}) &\approx \sum_{ij} \int e^{-it(\mathbf{z}' - \mathbf{z}) \cdot \Xi_{ij}^{DSA H}(s', s, \mathbf{z})} Q_{ij}^{DSA H}(\mathbf{z}, t, s', s) \\ &\quad \times A_{ij}^{DSA H}(\mathbf{z}, t, s', s) R_\rho(\mathbf{z}') dt ds dz' ds'. \end{aligned} \quad (1.50)$$

Note that under the assumptions (1.44) and (1.25), (1.50) shows that $\mathcal{K}_{ij}^{DSA H} \mathcal{F}_{ij}^{DSA H}$ is a pseudodifferential operator [33]. This means that the backprojection operator re-

Fig. 1.4 An illustration of the vector $\Xi_{ij}^{DSAH}(s', s, \mathbf{z})$ in the data collection manifold $\Omega_{ij, \mathbf{z}}^{DSAH}$ for the flat topography, $\psi(\mathbf{z}) = 0$. $\Xi_{ij}^{DSAH}(s', s, \mathbf{z})$ is the projection of the difference of the scaled vectors $\dot{\gamma}_{i, \perp}(s')$ and $\dot{\gamma}_{j, \perp}(s)$ onto the tangent plane of the ground topography at \mathbf{z} . (See (1.48) for an explicit form of $\Xi_{ij}^{DSAH}(s', s, \mathbf{z})$).



constructs the visible edges of the scene radiance at the correct location and correct orientation.

1.3.2 SAH Filtered-Backprojection Operator

For SAH imaging, we form an image of the scene radiance as follows:

$$\tilde{R}_p^{SAH}(\mathbf{z}) = \sum_{ij} \int \mathcal{K}_{ij}^{SAH}[E[d_{ij}]](\mathbf{z}, s') ds', \quad (1.51)$$

where we define

$$\mathcal{K}_{ij}^{SAH}[E[d]](\mathbf{z}, s') = \sum_{ij} \int e^{i\phi_{ij}^{SAH}(\omega, \mathbf{z}, s, s', \tau)} Q_{ij}^{SAH}(\mathbf{z}, \omega, s', s) d(s', s, \tau) d\tau d\omega ds ds'. \quad (1.52)$$

We refer to \mathcal{K}_{ij}^{SAH} as the SAH filtered-backprojection operator with respect to the i th and j th receivers with filter Q_{ij}^{SAH} to be determined below.

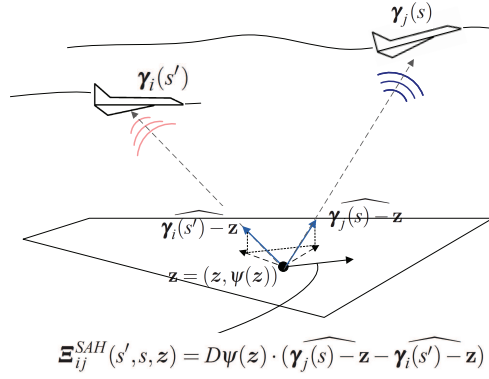
Similarly, we assume that for some m_Q^{SAH} , Q_{ij}^{SAH} satisfies the inequality

$$\sup_{(\omega, s', s, \mathbf{z}) \in K_{SAH}} \left| \partial_\omega^{\alpha_\omega} \partial_{s'}^{\beta_1} \partial_s^{\beta_2} \partial_{z_1}^{\epsilon_1} \partial_{z_2}^{\epsilon_2} Q_{ij}^{SAH}(\mathbf{z}, \omega, s', s) \right| \leq C_Q^{SAH} (1 + \omega^2)^{(m_Q^{SAH} - |\alpha_\omega|)/2}, \quad (1.53)$$

where K_{SAH} is any compact subsets of $\mathbb{R} \times \mathbb{R} \times \mathbb{R} \times \mathbb{R}^2$, and the constant C_Q^{SAH} depends on K_{SAH} , α_ω , $\beta_{1,2}$, $\epsilon_{1,2}$. The assumption in (1.53) makes \mathcal{K}_{ij}^{SAH} an FIO.

Substituting (1.36) into (1.52), and using the stationary phase theorem as in DSAH imaging, we approximate

Fig. 1.5 An illustration of the vector $\Xi_{ij}^{SAH}(s', s, \mathbf{z})$ in the data collection manifold $\Omega_{ij, \mathbf{z}}^{SAH}$ for the flat topography, $\psi(\mathbf{z}) = 0$. $\Xi_{ij}^{SAH}(s', s, \mathbf{z})$ is the projection of the difference of the unit vectors $\widehat{\boldsymbol{\gamma}_j(s) - \mathbf{z}}$ and $\widehat{\boldsymbol{\gamma}_i(s') - \mathbf{z}}$ onto the tangent plane of the ground topography at \mathbf{z} . (See (1.56) for an explicit form of $\Xi_{ij}^{SAH}(s', s, \mathbf{z})$).



$$\begin{aligned} \tilde{R}_\rho^{SAH}(\mathbf{z}) &= \sum_{ij} \mathcal{K}_{ij}^{SAH} \mathcal{F}_{ij}^{SAH}[R_\rho](\mathbf{z}) \\ &= \int e^{i\omega[r_{ij}(s', s, \mathbf{z}') - r_{ij}(s', s, \mathbf{z})]/c_0} Q_{ij}^{SAH}(\mathbf{z}, \omega, s', s) \\ &\quad \times A_{ij}^{SAH}(\mathbf{z}', \omega, s', s) R_\rho(\mathbf{z}') d\omega ds ds' dz'. \end{aligned} \quad (1.54)$$

We linearize $r_{ij}(s', s, \mathbf{z}')$ around $\mathbf{z}' = \mathbf{z}$ and make the following approximations:

$$r_{ij}(s', s, \mathbf{z}') - r_{ij}(s', s, \mathbf{z}) = (\mathbf{z}' - \mathbf{z}) \cdot \Xi_{ij}^{SAH}(s', s, \mathbf{z}), \quad (1.55)$$

where

$$\Xi_{ij}^{SAH}(s', s, \mathbf{z}) = D\psi(\mathbf{z}) \cdot (\widehat{\boldsymbol{\gamma}_j(s) - \mathbf{z}} - \widehat{\boldsymbol{\gamma}_i(s') - \mathbf{z}}) \quad (1.56)$$

and $D\psi(\mathbf{z})$ is given in (1.49).

For flat topography, we present an illustration of $\Xi_{ij}^{SAH}(s', s, \mathbf{z})$ in Figure (1.5).

Substituting (1.55) into (1.54), we obtain

$$\begin{aligned} \tilde{R}_\rho^{SAH}(\mathbf{z}) &= \sum_{ij} \int e^{i\omega(\mathbf{z}' - \mathbf{z}) \cdot \Xi_{ij}^{SAH}(s', s, \mathbf{z})/c_0} Q_{ij}^{SAH}(\mathbf{z}, \omega, s', s) \\ &\quad \times A_{ij}^{SAH}(\mathbf{z}', \omega, s', s) R_\rho(\mathbf{z}') d\omega ds ds' dz'. \end{aligned} \quad (1.57)$$

Under the assumptions (1.53) and (1.40), (1.57) shows that $\mathcal{K}_{ij}^{SAH} \mathcal{F}_{ij}^{SAH}$ is a pseudodifferential operator [33]. This means that the backprojection operator reconstructs the visible edges of the scene radiance at the correct location and orientation in SAH imaging.

1.3.3 Determination of the Filter

Q_{ij}^{DSAH} and Q_{ij}^{SAH} can be determined with respect to various criteria [40]. Ideally, they are chosen such that the leading-order contributions of the Point Spread Func-

tions (PSFs) of \mathcal{K}_{ij}^{DSAH} and \mathcal{K}_{ij}^{SAH} are Dirac-delta functions. This choice of the filters ensures that \mathcal{K}_{ij}^{DSAH} and \mathcal{K}_{ij}^{SAH} reconstruct the visible edges of the scene radiance not only at the correct location and orientation, but also with the correct strength [25, 26, 30, 40].

In DSAH imaging, for each s' and z , we make the following change of variables:

$$(t, s) \rightarrow \xi_{ij}^{DSAH} = t \Xi_{ij}^{DSAH}(s', s, z) \quad (1.58)$$

in (1.50) and obtain

$$\begin{aligned} \tilde{R}_\rho^{DSAH}(z) &\approx \sum_{ij} \int_{\Omega_{ij,s',z}^{DSAH}} e^{-i(z'-z) \cdot \xi_{ij}^{DSAH}} Q_{ij}^{DSAH}(z, t(\xi_{ij}^{DSAH}), s', s(\xi_{ij}^{DSAH})) \\ &\quad \times A_{ij}^{DSAH}(z, t(\xi_{ij}^{DSAH}), s', s(\xi_{ij}^{DSAH})) \left| \frac{\partial(t, s)}{\partial \xi_{ij}^{DSAH}} \right| R_\rho(z') d\xi_{ij}^{DSAH} dz' ds', \end{aligned} \quad (1.59)$$

where $|\partial(t, s)/\partial \xi_{ij}^{DSAH}|$ is the determinant of the Jacobian that comes from the change of variables given in (1.58).

The domain of integration in (1.59) is given as follows:

$$\Omega_{ij,s',z}^{DSAH} = \{ \xi_{ij}^{DSAH} = t \Xi_{ij}^{DSAH}(s', s, z) \mid A_{ij}^{DSAH}(z, t, s', s) \neq 0, (t, s', s) \in (\mathbb{R}, \mathbb{R}, \mathbb{R}) \}. \quad (1.60)$$

We refer to $\Omega_{ij,s',z}^{DSAH}$ as the DSAH *partial data collection manifold* at (s', z) obtained by the i th and j th receivers for a fixed s' and refer to the union $\cup_{ij,s'} \Omega_{ij,s',z}^{DSAH}$ as the DSAH *data collection manifold* at z and denote it by Ω_z^{DSAH} . This set determines many of the properties of the reconstructed DSAH image.

To approximate the PSF with the Dirac-delta function, we choose the the filter as follows:

$$Q_{ij}^{DSAH}(z, t, s', s) = \frac{A_{ij}^{DSAH*}(z, t, s', s, \mu) \chi_{\Omega_{ij,s',z}^{DSAH}}(z, t, s', s)}{|A_{ij}^{DSAH}(z, t, s', s, \mu)|^2 |\partial(t, s)/\partial \xi_{ij}^{DSAH}|}, \quad (1.61)$$

where $\chi_{\Omega_{ij,s',z}^{DSAH}}$ is a smooth cut-off function that is equal to one in the interior of $\Omega_{ij,s',z}^{DSAH}$ and zero in the exterior of $\Omega_{ij,s',z}^{DSAH}$.

Similarly, in SAH Imaging, for each s' and z , we make the following change of variables:

$$(\omega, s) \rightarrow \xi_{ij}^{SAH} = \frac{\omega}{c_0} \Xi_{ij}^{SAH}(s', s, z) \quad (1.62)$$

in (1.57) and obtain

$$\tilde{R}_\rho^{SAH}(z) \approx \sum_{ij} \int_{\Omega_{ij,s',z}^{SAH}} e^{i(z'-z) \cdot \xi_{ij}^{SAH}} Q_{ij}^{SAH}(z, \omega(\xi_{ij}^{SAH}), s', s(\xi_{ij}^{SAH}))$$

$$\times A_{ij}^{DSAH}(z, \omega(\xi_{ij}^{SAH}), s', s(\xi_{ij}^{SAH})) \left| \frac{\partial(\omega, s)}{\partial \xi_{ij}^{SAH}} \right| R_\rho(z') d\xi_{ij}^{SAH} dz' ds', \quad (1.63)$$

where $\left| \frac{\partial(\omega, s)}{\partial \xi_{ij}^{SAH}} \right|$ is the determinant of the Jacobian that comes from the change of variables in (1.62).

In (1.63), the domain of integration is given as follows:

$$\Omega_{ij, s', z}^{SAH} = \{ \xi_{ij}^{SAH} = \frac{\omega}{c_0} \Xi_{ij}^{SAH}(s', s, z) \mid A_{ij}^{SAH}(z, \omega, s', s) \neq 0, (\omega, s', s) \in (\mathbb{R}, \mathbb{R}, \mathbb{R}) \}. \quad (1.64)$$

We refer to $\Omega_{ij, s', z}^{SAH}$ as the SAH *partial data collection manifold* at (s', z) obtained by the i th and j th receivers for a fixed s' and refer to the union $\cup_{ij, s'} \Omega_{ij, s', z}^{SAH}$ as the SAH *data collection manifold* at z and denote it by Ω_z^{SAH} . Again, this set determines many of the properties of the reconstructed SAH image.

Similarly, to approximate the PSF with the Dirac-delta function, we choose the filter as follows:

$$\mathcal{Q}_{ij}^{SAH}(z, \omega, s', s) = \frac{A_{ij}^{SAH*}(z, \omega, s', s) \chi_{\Omega_{ij, s', z}^{SAH}}(z, \omega, s', s)}{|A_{ij}^{SAH}(z, \omega, s', s)|^2 |\partial(\omega, s)/\partial \xi_{ij}^{SAH}|}, \quad (1.65)$$

where $\chi_{\Omega_{ij, s', z}^{SAH}}$ is a smooth cut-off function that is equal to one in the interior of $\Omega_{ij, s', z}^{SAH}$ and zero in the exterior of $\Omega_{ij, s', z}^{SAH}$.

Irrespective of the choice of the filters, the filtered-backprojection operators \mathcal{K}_{ij}^{DSAH} and \mathcal{K}_{ij}^{SAH} reconstruct the visible edges of the scene radiance at the correct location and correct orientation. With the choice of the filters given in (1.61) and (1.65), the resulting image formation method can recover the visible edges not only at the correct location and orientation, but also with the correct strengths.

1.4 Resolution analysis

Substituting (1.61) and (1.65) into (1.59) and (1.63), respectively, we obtain

$$\tilde{R}_\rho^{DSAH}(z) \approx \sum_{ij} \int_{\Omega_{ij, s', z}^{DSAH}} e^{-i(z'-z) \cdot \xi_{ij}^{DSAH}} R_\rho(z') dz' d\xi_{ij}^{DSAH} ds', \quad (1.66)$$

$$\tilde{R}_\rho^{SAH}(z) \approx \sum_{ij} \int_{\Omega_{ij, s', z}^{SAH}} e^{i(z'-z) \cdot \xi_{ij}^{SAH}} R_\rho(z') dz' d\xi_{ij}^{SAH} ds'. \quad (1.67)$$

(1.66) and (1.67) show that the DSAH and SAH images, \tilde{R}_ρ^{DSAH} and \tilde{R}_ρ^{SAH} are bandlimited versions of R_ρ whose bandwidth are determined by the data collection

manifolds Ω_z^{DSAH} and Ω_z^{SAH} , respectively. The data collection manifolds determine the resolution of the reconstructed images at z . The larger the data collection manifold, the better the resolution of the reconstructed image is.

Microlocal analysis of (1.66) and (1.67) tell us that an edge at point z is visible in DSAH or SAH image if the direction \mathbf{n}_z normal to the edge is contained in Ω_z^{DSAH} or Ω_z^{SAH} , respectively [25, 26, 30, 40]. Consequently, an edge at point z with \mathbf{n}_z normal to edge is visible if there exists i, j, s', s such that ξ_{ij}^{DSAH} or ξ_{ij}^{SAH} is parallel to \mathbf{n}_z .

The bandwidth contribution of ξ_{ij}^{DSAH} and ξ_{ij}^{SAH} to a visible edge at z is given by

$$\frac{\omega_0}{c_0} L_\phi \left| D\psi(z) \cdot \left[\frac{1}{|\boldsymbol{\gamma}_i(s') - \mathbf{z}|} \dot{\boldsymbol{\gamma}}_{i,\perp}(s') - \frac{S_{ij}(s', s, z)}{|\boldsymbol{\gamma}_j(s) - \mathbf{z}|} \dot{\boldsymbol{\gamma}}_{j,\perp}(s) \right] \right|, \quad (1.68)$$

$$\frac{B_\omega}{c_0} \left| D\psi(z) \cdot (\widehat{\boldsymbol{\gamma}_j(s) - \mathbf{z}} - \widehat{\boldsymbol{\gamma}_i(s') - \mathbf{z}}) \right|, \quad (1.69)$$

where L_ϕ denotes the length of the support of $\phi(t)$ and B_ω denotes the bandwidth of the transmitted waveform.

(1.68) shows that for DSAH imaging, the longer the support of $\phi(t)$ becomes, the larger the magnitude of ξ_{ij}^{DSAH} is, giving rise to sharper reconstructed edges perpendicular to ξ_{ij}^{DSAH} , $i, j = 1, \dots, N$. Additionally, the higher the carrier frequency of the transmitted signal ω_0 becomes, larger the magnitude of ξ_{ij}^{DSAH} is, contributing to higher image resolution.

(1.69) shows that for SAH imaging, as the bandwidth of the transmitted signal becomes larger, the magnitude of ξ_{ij}^{SAH} gets larger, which results in higher image resolution. The sharpness of the reconstructed edges is also directly proportional to the bandwidth of the transmitted signal.

Furthermore, we note that in DSAH imaging, the resolution depends on the range via the terms $|\boldsymbol{\gamma}_i(s') - \mathbf{z}|$ and $|\boldsymbol{\gamma}_j(s) - \mathbf{z}|$ and the velocities of the receivers via the terms $\dot{\boldsymbol{\gamma}}_{i,\perp}$ and $\dot{\boldsymbol{\gamma}}_{j,\perp}$. As the scatterers are further away from the receivers, or the velocities of the receivers decrease, the resolution gets worse due to the decrease in the magnitude of ξ_{ij}^{DSAH} . In SAH imaging, the resolution also depends on the angle between the unit vectors $\widehat{\boldsymbol{\gamma}_j(s) - \mathbf{z}}$ and $\widehat{\boldsymbol{\gamma}_i(s') - \mathbf{z}}$. The larger the angle is, the larger the magnitude of ξ_{ij}^{SAH} becomes, resulting in better resolution.

Additionally, the increase in the number of s samples and the time windows (indicated by s') used for imaging also leads to a larger data collection manifold in DSAH or SAH imaging, which improves the resolution.

We summarize the parameters that affect the resolution of the reconstructed image in DSAH and SAH imaging in Table 1.1 and Table 1.2, respectively.

Table 1.1 Parameters that affect the DSAH image resolution

Parameter	Increase	Resolution
Carrier frequency: ω_0	↑	↑
Length of the windows L_ϕ	↑	↑
Distance $ \boldsymbol{\gamma}_i(s') - \mathbf{z} , \boldsymbol{\gamma}_j(s) - \mathbf{z} $	↑	↓
Antenna velocity $\dot{\boldsymbol{\gamma}}_i$ or $\dot{\boldsymbol{\gamma}}_j$	↑	↑
Number of s samples	↑	↑
Number of time windows (s')	↑	↑

↑: Increase (Higher) ↓: Decrease (Lower)

Table 1.2 Parameters that affect the SAH image resolution

Parameter	Increase	Resolution
Bandwidth of the transmitted waveform: B_ω	↑	↑
Angle between $\widehat{\boldsymbol{\gamma}_j(s) - \mathbf{z}}$ and $\widehat{\boldsymbol{\gamma}_i(s') - \mathbf{z}}$	↑	↑
Number of s samples	↑	↑
Number of time windows (s')	↑	↑

↑: Increase (Higher) ↓: Decrease (Lower)

1.5 Numerical Simulations

We considered a scene of size $[0, 22] \times [0, 22]$ km² with flat topography. The scene was discretized into 128×128 pixels, where $[0, 0, 0]$ km and $[22, 22, 0]$ km correspond to the pixels $(1, 1)$ and $(128, 128)$, respectively.

In all the numerical experiments, we used two airborne receivers and a single, stationary transmitter operating either cooperatively or non-cooperatively. We assumed that both the receiver and transmitter antennas were isotropic. We assumed that the transmitter was located at $\mathbf{y}_0 = (0, 0, 6.5)$ km and the receivers were traversing the circular trajectory given by

$$\boldsymbol{\gamma}_C(\tilde{s}) = (11 + 11 \cos(\tilde{s}), 11 + 11 \sin(\tilde{s}), 6.5) \text{ km.} \quad (1.70)$$

Let $\boldsymbol{\gamma}_1(\tilde{s})$ and $\boldsymbol{\gamma}_2(\tilde{s})$ denote the trajectories of the two receivers. We set $\boldsymbol{\gamma}_1(\tilde{s}) = \boldsymbol{\gamma}_C(\tilde{s})$ and $\boldsymbol{\gamma}_2(\tilde{s}) = \boldsymbol{\gamma}_1(\tilde{s} - \frac{\pi}{6})$. Note that the variable \tilde{s} in $\boldsymbol{\gamma}_C$ is equal to $\frac{V}{R}t$, where V is the speed of the receiver, and R is the radius of the circular trajectory. We set the speed of the two receivers to 261 m/s. We chose the sampling rate of s to be 1.9335Hz so as to uniformly sample the circular trajectory with 512 points.

In accordance with the incoherent field approximation, we used the following multiple-point-target model for the scene reflectivity,

$$\rho(\mathbf{z}) = \sum_{l=1}^L g_l \delta(\mathbf{z} - \mathbf{z}_l), \quad (1.71)$$

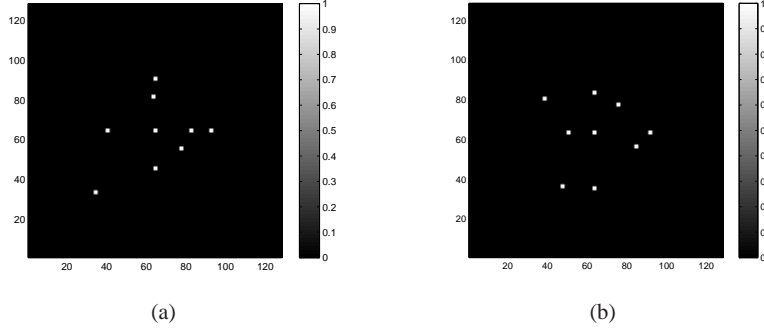
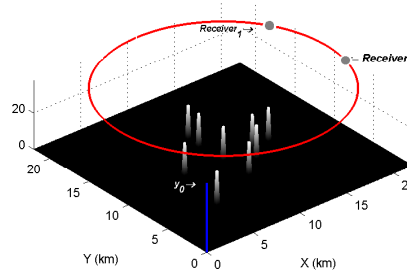


Fig. 1.6 Discretized scene reflectivity used in the numerical simulations of (a) DSAH imaging and (b) SAH imaging. $[0, 0, 0]$ km and $[22, 22, 0]$ km are located at the lower left and upper right corners, respectively.

Fig. 1.7 3-D view of the scene with multiple point targets, illuminated by a single transmitter located at $\mathbf{y}_0 = (0, 0, 6.5)$ km and the circular receiver trajectory $\gamma_C(\bar{s}) = (11 + 11 \cos(\bar{s}), 11 + 11 \sin(\bar{s}), 6.5)$ km, as shown by the red solid line. At a certain time instant, two receivers are located at the positions shown in the figure.



where g_l , $l = 1, \dots, L$ are independent Gaussian random variables with mean μ_l and variance σ_l^2 . The corresponding scene radiance is given by

$$R_\rho(\mathbf{z}) = E[\rho(\mathbf{z})\rho^*(\mathbf{z})] = \sum_l (\mu_l^2 + \sigma_l^2) \delta(\mathbf{z} - \mathbf{z}_l). \quad (1.72)$$

In our simulations, we considered a deterministic reflectivity and set $\sigma_l^2 = 1$. We used $L = 9$ and approximated the Dirac-delta functions in (1.72) by square target reflectors of size 344×344 m², each having a unit reflectivity, i.e., $\mu_l = 1$, $l = 1, \dots, 9$.

Figure 1.6(a) and Figure 1.6(b) show the scene with targets used in the simulations of the DSAH imaging and SAH imaging, respectively. Figure 1.7 shows the receiver trajectories and the transmitter antenna location used for DSAH and SAH simulations.

We performed image reconstruction for each s' and coherently superimposed the reconstructed images obtained over a range of s' .

1.5.1 Numerical Simulations for DSAH imaging

We used (1.9) to generate the data and chose the windowing function ϕ in (1.9) to be a Hanning function.

The transmitted waveform was assumed to be a single frequency CW waveform with 800MHz carrier frequency. The length of the windowing function was set to $L_\phi = 0.0853s$.

For the case of a cooperative transmitter, the reconstructed image is shown in Figure 1.8(a). It can be seen that the targets are well reconstructed using the DSAH image formation method.

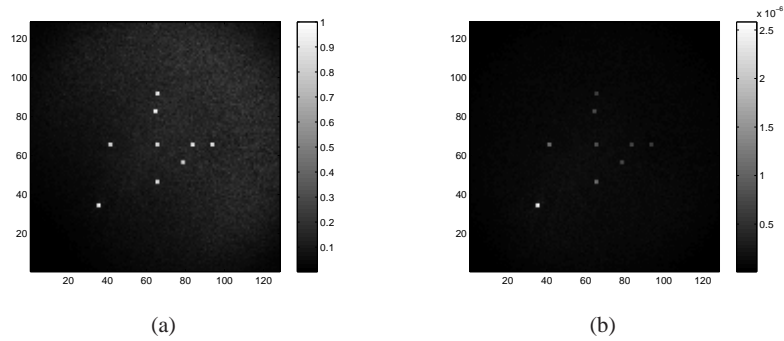


Fig. 1.8 The reconstructed DSAH images obtained by superposing the images obtained using multiple s' values and two receivers traversing the circular flight trajectories $\gamma_1(\vec{s})$ and $\gamma_2(\vec{s})$ as shown in Figure 1.7 and a single (a) cooperative transmitter, and (b) noncooperative transmitter located at \mathbf{y}_0 .

Figure 1.8(b) shows the reconstructed image using a non-cooperative transmitter. Since the location of the transmitter was assumed to be unknown, the received signal was not compensated for the transmitter related geometric spreading factors. As a result, the targets closer to the transmitter appears brighter in the reconstructed image than those that are further away from the transmitter.

1.5.2 Numerical Simulations for SAH imaging

We used (1.33) to generate the data for performing SAH imaging simulations and chose the windowing function ϕ in (1.33) to be a Hanning function as in DSAH imaging simulations.

A transmitted pulse at center frequency 0Hz with bandwidth equal to 0.873MHz was used in the simulations.

The reconstructed images corresponding to the cooperative and non-cooperative transmitter cases are shown in Figure 1.9(a) and Figure 1.9(b), respectively. We

see that the targets are reconstructed successfully in both cases and in the non-cooperative case, the strength of the targets closer to the transmitter are higher as expected.

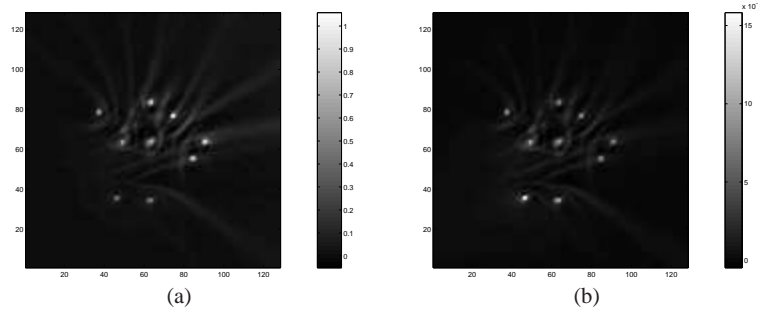


Fig. 1.9 The reconstructed SAH images obtained by superposing the images obtained using multiple s' values and two receivers traversing the circular flight trajectories $\gamma_1(\vec{s})$ and $\gamma_2(\vec{s})$ as shown in Figure 1.7 and a single (a) cooperative transmitter, and (b) noncooperative transmitter located at y_0 .

1.6 Conclusion

We presented a unified theory of passive synthetic aperture imaging based on inverse scattering theory, estimation-detection theory and microlocal analysis. Our theory involves development of passive measurement models based on inverse scattering and estimation-detection theory and analytic inversion methods based on microlocal analysis. The measurement models involve windowed, scaled and translated correlation of the received signals at different receiver locations. This correlation process results in measurement models in the form of FIOs. Taking into account the nature of the waveforms of opportunity, we developed two different measurement models: DSAH FIO and SAH FIO.

DSAH FIO-based model projects the scene radiance onto passive iso-Doppler contours, and SAH FIO-based model projects the scene radiance onto passive iso-range contours. The correlation process removes the transmitter related terms from the phase of the resulting FIO-based DSAH and SAH measurement models, allowing us to perform backprojection without the knowledge of the transmitter locations.

We used microlocal techniques to backproject the correlated signals onto the passive iso-Doppler contours in DSAH imaging and onto passive iso-range contours in SAH imaging. The filtered-backprojection reconstruction methods for DSAH and SAH have the desirable property of preserving the visible edges of the scene radiance at the correct location and orientation, and at the correct strength with appropriate choice of filters.

Our analysis shows that the resolution of the reconstructed DSAH images is determined primarily by the temporal duration and frequency of the transmitted waveforms, and the resolution of the reconstructed SAH images is determined primarily by the bandwidth of the transmitted waveforms. These results are consistent with the ambiguity theory of the CW or ultra-narrowband waveforms and the wideband waveforms.

While we focused primarily on the passive synthetic aperture radar, the theory of DSAH and SAH imaging introduced in this Chapter and the resulting methods and algorithms are also applicable to other wave-based passive imaging problems, such as those that arise in geophysics or acoustics.

References

1. Antoniou, M., Cherniakov, M., Hu, C.: Space-surface bistatic sar image formation algorithms. *IEEE Transactions on Geoscience and Remote Sensing* **47**(6), 1827–1843 (2009)
2. Baker, C.J., Griffiths, H.D., Papoutsis, I.: Passive coherent location radar systems. part 2: Waveform properties. *IEE Proc.-Radar Sonar Navig.* **152**(3), 160–168 (2005)
3. Barrett, H., Myers, K.: *Foundations of image science*. Wiley-Interscience, Hoboken, NJ (2004)
4. Bleistein, N., Handelsman, R.: *Asymptotic Expansions of Integrals*. Dover, New York (1986)
5. Chetty, K., Woodbridge, K., Guo, H., Smith, G.E.: Passive bistatic WiMAX radar for marine surveillance. In: *Proc. of 2010 IEEE Radar Conference* (2010)
6. Christiansen, J.M., Olsen, K.E.: Range and doppler walk in DVB-T based passive bistatic radar. In: *Proc. of 2010 IEEE Radar Conference* (2010)
7. Coleman, C., Yardley, H.: Passive bistatic radar based on target illuminations by digital audio broadcasting. *IET Radar Sonar Navig.* **2**(5), 366–375 (2008)
8. Demanet, L., Ferrara, M., Maxwell, N., Poulson, J., Ying, L.: A butterfly algorithm for synthetic aperture radar imaging. submitted to *SIAM Journal on Imaging Science* (2010)
9. Falcone, P., Colone, F., Bongioanni, C., Lombardo, P.: Experimental results for OFDM WiFi-based passive bistatic radar. In: *Proc. of 2010 IEEE Radar Conference* (2010)
10. Garnier, J., Papanicolaou, G.: Passive imaging using cross correlations of ambient noise signals. In: *Proc. of 2009 3rd IEEE Int. workshop on Computational Advances in Multi-Sensor Adaptive Processing (CAMSAP)*, pp. 221–224 (2009)
11. Garnier, J., Papanicolaou, G.: Passive sensor imaging using cross correlations of noisy signals in a scattering medium. *SIAM J. Imaging Sci.* **2**(2), 396–437 (2009)
12. Garnier, J., Papanicolaou, G.: Resolution analysis for imaging with noise. *Inverse Problems* **26** (074001) (2010)
13. Garnier, J., Solna, K.: Passive imaging and detection in cluttered media. In: *Proc. of 2009 3rd IEEE Int. workshop on Computational Advances in Multi-Sensor Adaptive Processing (CAMSAP)*, pp. 225–228 (2009)
14. Griffiths, H.D., Baker, C.J.: Passive coherent location radar systems. part 1: Performance prediction. *IEE Proc.-Radar Sonar Navig.* **152**(3) (2005)
15. Grigis, A., Sjöstrand, J.: *Microlocal Analysis for Differential Operators: An Introduction*. London Mathematical Society Lecture Note Series, Vol. 196. Cambridge University Press, Cambridge (1994)
16. Guillemin, V., Sternberg, S.: *Geometric Asymptotics*. American Math. Society, Providence (1979)
17. Guo, H., Woodbridge, K., Baker, C.J.: Evaluation of WiFi beacon transmissions for wireless based passive radar. In: *Proc. of 2008 IEEE Radar Conference* (2008)
18. Harms, H.A., Davis, L.M., Palmer, J.: Understanding the signal structure in DVB-T signals for passive radar detection. In: *Proc. of 2010 IEEE Radar Conference* (2010)

19. Homer, J., Kubik, K., Mojarrabi, B., Longstaff, I., Donskoi, E., Cherniakov, M.: Passive bistatic radar sensing with leos based transmitters. In: Proceedings of IEEE International Geoscience and Remote Sensing Symposium, vol. 1, pp. 438–440 (2002)
20. Howland, P.E., Maksimiuk, D., Reitsma, G.: Fm radio based bistatic radar. IEE Proceedings of Radar, Sonar and Navigation **152**(3), 107–115 (2005)
21. Kay, S.M.: Fundamentals of Statistical Signal Processing, Vol. I and Vol. II. Prentice Hall (1998)
22. Lenanon, N., Mozeson, E.: Radar Signals. Wiley-IEEE Press (2004)
23. Li, G., Xu, J., Peng, Y.N., Xia, X.G.: Bistatic linear array SAR for moving target detection, location and imaging with two passive airborne radars. IEEE Transactions on Geoscience and Remote Sensing **45**(3), 554–565 (2007)
24. Natterer, F., Wübbeling, F.: Mathematical methods in image reconstruction. SIAM, Philadelphia, PA (2001)
25. Nolan, C., Cheney, M.: Synthetic aperture inversion for arbitrary flight paths and non-flat topography. IEEE Transactions on Image Processing **12**, 1035–1043 (2003)
26. Nolan, C.J., Cheney, M.: Synthetic aperture inversion. Inverse Problems **18**, 221–236 (2002)
27. O’Hagan, D.W., Baker, C.J.: Passive bistatic radar (PBR) using FM radio illuminators of opportunity. In: Proc. of 2008 IEEE Radar Conference (2008)
28. Pollard, R.: The role of passive radar sensors for air traffic control. In: The Institution of Engineering and Technology Seminar on the Future of Civil Radar (2006)
29. Poullin, D.: Passive detection using digital broadcasters (DAB, DVB) with COFDM modulation. IEE Proc.-Radar Sonar Navig. **152**(3), 143–152 (2005)
30. Quinto, E.: Singularities of the x-ray transform and limited data tomography in r^2 and r^3 . SIAM J. Math. Anal. **24**, 1215–1225 (1993)
31. Skolnik, M.I.: Introduction to Radar Systems, Third Edition. McGraw-Hill (2002)
32. Tan, D., Sun, H., Lu, Y., Lesturgie, M., Chan, H.L.: Passive radar using global system for mobile communication signal: theory, implementation and measurements. IEE Proc.-Radar Sonar Navig. **152**(3), 116–123 (2005)
33. Treves, F.: Introduction to Pseudodifferential and Fourier Integral Operators, volumes I and II. Plenum Press, New York (1980)
34. Veen, B.D.V., Buckley, K.M.: Beamforming: A versatile approach to spatial filtering. IEEE ASSP Magazine pp. 4–24 (1988)
35. Voccola, K., Yazıcı, B., Cheney, M., Ferrara, M.: On the equivalence of the generalized likelihood ratio test and backprojection method in synthetic aperture imaging. In: Proc. SPIE on Defense and Security Conference, vol. 7335, pp. 1Q1–10 (2009)
36. Wang, L., Son, I.Y., Yazıcı, B.: Passive imaging using distributed apertures in multiple scattering environments. Inverse Problems **26** (065002) (2010)
37. Woodward, P.M.: Radar Ambiguity Analysis. Technical Note No.731 (1967)
38. Yarman, C., Wang, L., Yazıcı, B.: Doppler synthetic aperture hitchhiker imaging. Inverse Problems **26** (065006), 26pp (2010)
39. Yarman, C., Yazıcı, B.: Synthetic aperture hitchhiker imaging. IEEE Transactions on Imaging Processing **17**(11), 2156–2173 (2008)
40. Yazıcı, B., Cheney, M., Yarman, C.: Synthetic-aperture inversion in the presence of noise and clutter. Inverse Problems **22**, 1705–1729 (2006)